Electrostatically Balanced Subnanometer Imaging of Biological Specimens by Atomic Force Microscope

Daniel J. Müller, Dimitrios Fotiadis, Simon Scheuring, Shirley A. Müller, and Andreas Engel
M. E. Müller-Institute for Microscopic Structural Biology, Biozentrum, University of Basel, Basel, Switzerland

ABSTRACT To achieve high-resolution topographs of native biological macromolecules in aqueous solution with the atomic force microscope (AFM) interactions between AFM tip and sample need to be considered. Short-range forces produce the submolecular information of high-resolution topographs. In contrast, no significant high-resolution information is provided by the long-range electrostatic double-layer force. However, this force can be adjusted by pH and electrolytes to distribute the force applied to the AFM tip over a large sample area. As demonstrated on fragile biological samples, adjustment of the electrolyte solution results in a local reduction of both vertical and lateral forces between the AFM tip and proteinous substructures. Under such electrostatically balanced conditions, the deformation of the native protein is minimized and the sample surface can be reproducibly contoured at a lateral resolution of 0.6 nm.

INTRODUCTION

Atomic force microscopy (Binnig et al., 1986) is now an established technique for imaging the surfaces of biological systems in their native environment at high resolution (Drake et al., 1989; Shao et al., 1996; Engel et al., 1997). Topographs of native proteins with a resolution down to the subnanometer scale demonstrate the power of this microscope (Butt et al., 1991; Hoh et al., 1993; Karrasch et al., 1994; Schabert and Engel, 1994; Mou et al., 1995; Müller et al., 1995b, 1997c; Mou et al., 1996; Walz et al., 1996; Czajkowsky et al., 1998a). Recently, the atomic force microscope (AFM) has been employed to measure forces between pairs of interacting biological molecules (Florin et al., 1994; Lee et al., 1994a,b; Moy et al., 1994; Dammer et al., 1995, 1996) and forces required for the unfolding of titin domains (Rief et al., 1997; Oberhauser et al., 1998). It is, furthermore, possible to image protein complexes before and after the removal of individual subunits using the AFM tip as a nanotool (Fotiadis et al., 1998). The ability to image conformational changes (Müller et al., 1995a, 1996b, 1997c,d) and to map the flexibilities of native proteins at subnanometer resolution (Müller et al., 1998) suggests that the dynamics of protein surfaces may in the future be directly observed and characterized using this microscope.

The interpretation of AFM topographs requires knowledge of the factors involved in image formation. Aspects such as the contrast transfer (Engel, 1991; Engel et al., 1997) and the interactions occurring between the AFM tip and the biological sample are of particular interest (Müller and Engel, 1997; Ho et al., 1998). The buffer solution necessary to preserve the native activity of a biological system also has a significant influence on AFM tip-sample (Butt, 1991a,b; 1992a,b) and sample-support interactions (Müller et al., 1997a,b). Differences in surface charge densities affect the electrostatic double-layer repulsion between tip-sample and tip-support, which causes the measured height of a biological sample to deviate from its actual thickness (Müller and Engel, 1997) and changes the phase lag between the driving and observed cantilever oscillation in tapping mode phase imaging (Czajkowsky et al., 1998b). Here we estimate the electrolyte concentration required to adjust the double-layer repulsion so that both vertical and lateral forces between the tip and the native biological system are minimized. This electrostatically balanced recording condition improves the spatial resolution of the AFM operated in contact mode.

Received for publication 1 September 1998 and in final form 4 November 1998.

Address reprint requests to Drs. Daniel J. Müller and Andreas Engel, M.E. Müller-Institute for Microscopic Structural Biology, Biozentrum, University of Basel, Klingelbergstrasse 70, CH-4056 Basel, Switzerland. Tel.: 0041-61-267-2261; Fax: 0041-61-267-2109; E-mail: muellerda@ubaclu.unibas.ch.

0006-3495/99/02/1101/11 $2.00

MATERIALS AND METHODS

Atomic force microscopy

A commercial AFM (Nanoscope III, Digital Instruments Inc., Santa Barbara, CA) equipped with a 120-μm scanner (j-scanner) and a liquid cell were employed. Before use, the liquid cell was cleaned with normal dish cleaner (Pril, Henkel Hygiene AG, Pratteln, Switzerland), gently rinsed with ultrapure water ($\approx$ 18 MΩ/cm; Branstead, Boston, MA), sonicated in ethanol (50 kHz), and sonicated in ultrapure water (50 kHz). Mica (Mica New York Corp., New York) was punched to a diameter of about 5 mm and glued onto a Teflon disc with water insoluble epoxy glue (Araldit, Ciba Geigy AG, Basel, Switzerland). The diameter of the Teflon disc (11 mm) was slightly larger than the diameter of its supporting steel disc. The steel disc was required to magnetically mount it onto the piezoelectric scanner. Imaging at low magnification (scan size $>$ 500 nm) was performed in the error signal mode. Acquisition of the deflection and height signals was simultaneous (Putman et al., 1992). The deflection signal was minimized by optimizing integral and proportional gains and scan speed. At high resolution (scan size $<$ 200 nm) topographs were scanned simultaneously in the trace and retrace directions. The scan speed was roughly linear to the scan size, 4 to 8 lines per second for lower magnifications (frame size, 1–25 μm). The applied force was corrected manually to compensate for thermal drift. The force constant of the 120-μm-long cantilevers purchased from Olympus Ltd. (Tokyo, Japan) was 0.1 N/m and of the 200-μm-long

cantilevers purchased from Digital Instruments Inc. (Santa Barbara, CA) it was 0.06 N/m. Both cantilevers had oxide-sharpened Si_3N_4 tips. Calibration of the piezo scanner was carried out using layered crystals such as transition metal dichalcogenides (Wilson and Yoffe, 1969) as references (Müller and Engel, 1997). All topographs were recorded in the contact mode at applied forces of 0.1 nN.

Biological samples

Hexagonally packed intermediate (HPI) layer of *Deinococcus radiodurans* had been extracted from whole cells (strain SARK) with sodium dodecyl sulfate and purified on a Percoll density gradient (Baumeister et al., 1982). Purple membranes of *Halobacterium salinarum* strain ET1001 had been isolated as described by Oesterhelt and Stoeckenius (1974). The membranes were frozen and stored in water at −70°C. After thawing, stock solutions (5 mg protein/ml) were kept in distilled water at 4°C. Porin OmpF trimers from *E. coli* strain BZ1110/PMY222 (Hoenger et al., 1993) solubilized in octyl-polyoxyethylene had been mixed with solubilized dimyristoyl phosphatidylcholine (99% purity, Sigma Chemical, St. Louis, MO) at a lipid-to-protein ratio (w/w) of 0.2 and a protein concentration of 1 mg/ml. This mixture had been reconstituted in a temperature-controlled dialysis device (Jap et al., 1992).

Image processing

For image processing, raw data (size, 512 × 512 pixels) acquired in the trace and retrace directions were transferred to a Digital Equipment Alpha workstation and analyzed using the Semper image processing system (Saxton et al., 1979). Residual lattice disorder was eliminated by correlation averaging (Saxton and Baumeister, 1982). As a final step correlation averaged unit cells were symmetrized. Derjaguin-Landau-Verwey-Overbeek (DLVO) forces were calculated using the program Kaleidagraph (Abelbeck Software).

Sample preparation

To minimize contamination of surfaces during exposure to ambient air, sample supports were prepared immediately before use. All buffers were made with ultrapure water (≈ 18 MΩ/cm). This water contains fewer hydrocarbons than conventional bi-distilled water and fewer macroscopic contaminants, all of which can influence the imaging process. Chemicals were p.a. grade and purchased from Sigma Chemie AG (Buchs, Switzerland). The buffer used was Tris-(hydroxymethyl)-aminomethane (Tris). The pH of all buffer solutions was adjusted at room temperature (22°C). The samples were checked by conventional negative stain electron microscopy (Bremer et al., 1992) and by biochemical techniques (e.g., sodium dodecyl sulfate polyacrylamide gel electrophoresis) before use.

The biological samples were diluted to a concentration of 5–20 μg/ml in buffer solution (10 mM Tris-HCl, 300 mM KCl, pH 7.6) before adsorption to freshly cleaved mica (Müller et al., 1997a). After an adsorption time of 15 to 60 min, the samples were gently washed with the imaging buffer as noted in the figure legends to remove nonadsorbed and weakly attached membranes.

RESULTS

High-resolution images of purple membrane depend on electrolyte concentrations

Fig. 1 presents topographs of the extracellular surface of purple membrane recorded under different electrolyte concentrations at a constant applied force of about 0.1 nN. When the extracellular surface was imaged in 150 mM KCl (10 mM Tris-HCl, pH 7.6), submolecular resolution was obtained (Fig. 1 *a*). Structural details in such high-resolution images recorded simultaneously in the trace and retrace directions were identical. This became especially clear when the correlation averages of 170 unit cells were compared (insets). Three main domains exhibiting horseshoe-like substructures per bacteriorhodopsin trimer were visible (Müller et al., 1996a). The smallest reproducible details resolved, indicated by an ellipse (Fig. 1 *a*, inset), were separated by about 1.2 nm and had a width at half maximum height of 0.6 nm. The average height of the main protrusions above the indicated substructures was 0.4 ± 0.1 nm (n = 143). After threefold symmetrization, the three major domains were arranged on an equilateral triangle of 2.8 nm

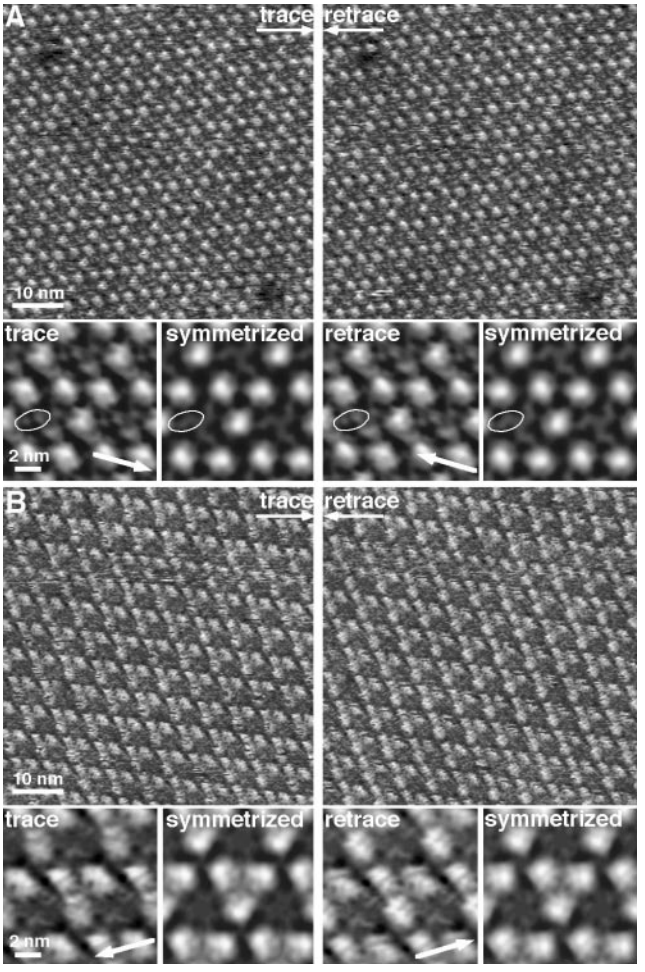

FIGURE 1 AFM topographs of the extracellular purple membrane surface recorded at subnanometer resolution under different electrolyte concentrations. (*a*) Extracellular surface imaged in the presence of 150 mM KCl (10 mM Tris-HCl, pH 7.6). Correlation averages from 170 unit cells are shown in the insets, with arrows indicating the scanning direction. The symmetrized averages (*insets*) have a root-mean-square (RMS) deviation from the threefold symmetry of 2.8%. (*b*) Extracellular surface imaged in the presence of 50 mM $MgCl_2$, 50 mM KCl (10 mM Tris-HCl, pH 7.6). Correlation averages from 193 unit cells are shown in the insets. The symmetrized averages (*insets*) showed a RMS deviation from the threefold symmetry of 6.1%. Topographs were recorded simultaneously in the trace and the retrace direction, applied forces of 0.1 nN and scan frequencies of 6.8 Hz. Full gray-level ranges: 1.5 nm (raw data) and 1 nm (*insets*).

side length (peak-to-peak distances). The minor protrusions, indicated by a white contour, became less pronounced after symmetrization and three such regions were symmetrically inscribed by an equilateral triangle of 2.0 nm side length.

Submolecular details were also observed when the imaging was performed at applied forces of 0.1 nN in 50 mM $MgCl_2$, 50 mM KCl (10 mM Tris-HCl, pH 7.6) (Fig. 1 *b*). However, the topographs simultaneously recorded in the trace and retrace directions were different, as clearly documented on comparison of the correlation averages from over 193 unit cells (insets). In this case, the two averages showed different substructures of the bacteriorhodopsin trimer, which appeared broadened and flattened. Although the identical tip was used as in Fig. 1 *a*, tip effects appeared to influence image formation. The main domains showed larger height variations, the average height above the minimum domains being 0.2 ± 0.2 nm ($n = 126$). The minor domains appeared to be smeared out. After threefold symmetrization, the three major domains were arranged on an equilateral triangle of 3.0 nm side length and the three minor domains were separated by 2.0 nm as before.

When the extracellular surface of purple membrane was imaged at applied forces of 0.1 nN in buffer solution with an electrolyte concentration of 20 mM KCl (5 mM Tris-HCl, pH 7.6), no structural details were observed (data not shown).

To investigate this electrolyte dependence, force curves were recorded on the extracellular surface of purple membrane (Fig. 2) directly after high-resolution imaging (Fig. 1). To this end, the cantilever was pushed toward the sample (from right to left in the force plot shown in Fig. 2) and its deflection simultaneously monitored. The force calculated from the deflection and spring constant of the cantilever (see Materials and Methods) is plotted along the vertical axis. Force curves recorded in the presence of 20 mM KCl (5 mM Tris-HCl, pH 7.6) indicated the effect of long-range repulsive forces (Fig. 2, top trace arrow 1) that arise from the electrostatic double-layer repulsion (Butt, 1992a,b; Müller and Engel, 1997). This electrostatic double-layer force rose smoothly as the distance between the tip and the membrane decreased. When the two surfaces came in contact, the force showed a linear dependence on further movement of the cantilever (Fig. 2, arrow 2). Force curves recorded in the presence of 50 mM KCl (10 mM Tris-HCl, pH 7.6) or 150 mM KCl (10 mM Tris-HCl, pH 7.6) also indicated repulsive forces (Fig. 2, arrow 1). But in these cases the repulsive dependence began closer to the membrane surface and showed a smaller maximum than in 20 mM KCl. The electrostatic repulsion was almost zero when 300 mM KCl (10 mM Tris-HCl, pH 7.6) was employed (Fig. 2, arrow 1) and was fully compensated at salt concentrations of 50 mM KCl and 50 mM $MgCl_2$ (10 mM Tris-HCl, pH 7.6) (Fig. 2, bottom trace). In the latter case, the tip was in contact with the biological sample at applied forces above 0.025 nN (noise of the AFM in our experiments).

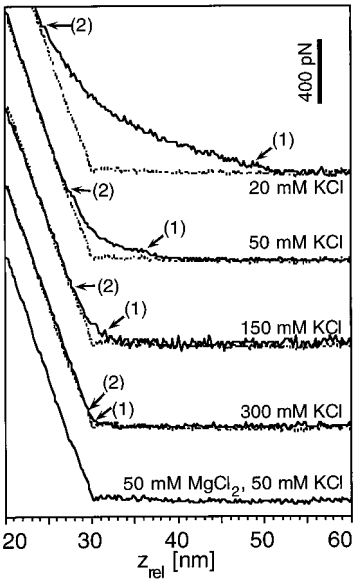

FIGURE 2 Force-distance curves recorded on the extracellular purple membrane surface. The data was obtained for different electrolyte concentrations at constant pH (7.6). Force curves were recorded during the approach of sample and AFM tip. The dotted lines (. . . .) represent force-distance curves recorded on purple membrane without electrostatic repulsion. Conditions: scan frequency 1.97 Hz, scan range 50 nm (512 pixels). Arrows (1) mark the onset of measurable electrostatic repulsion, whereas arrows (2) indicate the point of contact between tip and sample.

Fig. 2 shows that the distance between AFM tip and purple membrane depends on both the applied force and the electrolyte used (Müller and Engel, 1997). The valency and concentration of the cations present influence the electrostatic double-layer interaction (Israelachvili, 1991). Clearly, the AFM tip is not in contact with the membrane if the repulsive double-layer force is higher than the applied force. However, as shown in Fig. 2, the repulsive force can be reduced by increasing the electrolyte concentration and valency (Butt, 1991a,b, 1992b; Ducker et al., 1991; Butt et al., 1995). To prevent deformations of native proteins during AFM imaging, the applied force must be $\leq$ 0.1 nN (Schabert et al., 1995; Müller et al., 1995a, 1996b, 1997c). Force curves allow the corresponding distance between tip and membrane during imaging at 0.1 nN to be estimated (Fig. 2) (Müller and Engel, 1997). Thus, in 20 mM KCl the separation was $\approx$ 18 nm, in 150 mM KCl it was $\approx$ 2 nm (compare Fig. 1 *a*), and in 50 mM $MgCl_2$, 50 mM KCl the tip was in contact with the membrane (compare Fig. 1 *b*). These results point out a dependence of spatial resolution and sample deformation on the tip-membrane separation when an applied force of 0.1 nN is used. The dependence on the ionic strength of the solution used suggests an influence of electrostatic forces during high-resolution imaging.

Electrostatic forces between AFM tip and sample

Biological macromolecules and the tips used for AFM exhibit a net surface charge in an aqueous environment. Since acidic and basic functional groups at their surface dissociate

according to their pK values, the magnitude and sign of this charge depend on the temperature and the pH of the system. In electrolyte solution it is compensated by counterions, which concentrate at the surface. According to Boltzmann's law the counterion concentration decays exponentially to the distance from the surface. This exponential decrease is characterized by the Debye length, λ_D, also understood as the thickness of the diffuse electrical double-layer formed by counterions. As shown in Eq. 1, λ_D depends only upon the ionic valency q_i and the concentration c_i of the *i*th electrolyte component of the liquid (Israelachvili, 1991):

$$\lambda_D = \sqrt{\frac{\epsilon_0 \epsilon_e kT}{e^2 \sum_i c_i q_i^2}} \tag{1}$$

where k is the Boltzmann constant, T is the absolute temperature, e is the unit charge, ϵ_0 is the permittivity of the vacuum, and ϵ_e is the dielectric constant of the medium, in this case water. Note the strong dependence of the double-layer thickness on the valency of the ions.

An electrostatic interaction arises when the electrical double-layers of the tip and the sample surfaces overlap. This occurs at separations of a few tens of nanometers. At smaller separations the van der Waals force must also be considered. The interplay between electrostatic forces (F_{el}) and van der Waals forces (F_{vdW}) can be described by the DLVO theory, neglecting effects of ionic radius, hydration forces, steric forces, and specific interactions (Israelachvili, 1991). Calculation of the DLVO forces (F_{DLVO}) between the AFM tip and the sample requires an estimate of the interacting surface area of the tip. Surface charge density measurements have demonstrated the global tip radius to be R_{glo} = 40–200 nm (Butt, 1992b; Müller and Engel, 1997). However, topographs of protein surfaces exhibiting subnanometer resolution suggest that a tip with a very small radius interacts locally with the protein. A quantitative comparison of topographs of porin OmpF acquired by AFM with the atomic structure (Cowan et al., 1992) yielded a radius for the protrusion of R_{loc} = 2 nm (Schabert and Engel, 1994).

The F_{DLVO} between a local protrusion and a spherical protein of comparable radius R_{loc} (see above) and that between a macroscopic sphere R_{glo} interacting with a planar surface, such as a purple membrane sheet, are given by Eqs. 2 and 3, respectively (Israelachvili, 1991):

$$F_{DLVO}^{loc}(z) = F_{el}(z) + F_{vdW}(z) = \frac{2\pi\sigma_s\sigma_t R_{loc}\lambda_D}{\epsilon_e\epsilon_0} e^{-z/\lambda_D} - \frac{H_a R_{loc}}{12z^2} \tag{2}$$

$$F_{DLVO}^{glo}(z) = F_{el}(z) + F_{vdW}(z) = \frac{4\pi\sigma_s\sigma_t R_{glo}\lambda_D}{\epsilon_e\epsilon_0} e^{-z/\lambda_D} - \frac{H_a R_{glo}}{6z^2} \tag{3}$$

where σ_s and σ_t are the surface charge densities of sample and tip, H_a is the Hamaker constant, and *z* is the distance between the two surfaces. To calculate the model of a microscopic half sphere located on a macroscopic tip, Eqs. 2 and 3 provide:

$$\begin{aligned} F_{DLVO}(z) &\approx F_{DLVO}^{glo}(z) + \frac{1}{2} F_{DLVO}^{loc}(z) \\ &= \frac{4\pi\sigma_s\sigma_t R_{glo}\lambda_D}{\epsilon_e\epsilon_0} e^{-(z+R_{loc})/\lambda_D} - \frac{H_a R_{glo}}{6(z+R_{loc})^2} \\ &\quad + \frac{\pi\sigma_s\sigma_t R_{loc}\lambda_D}{\epsilon_e\epsilon_0} e^{-z/\lambda_D} - \frac{H_a R_{loc}}{24z^2} \end{aligned} \tag{4}$$

The shape and the surface properties of both the AFM tip and the sample define the electrostatic double-layer interaction (depending on surface charge density), and the van der Waals attraction characterized by the Hamaker constant (Israelachvili, 1991). Whereas F_{vdW} is mainly unaffected by the electrolyte concentration and pH of the buffer solution, F_{el} depends on these variables. Thus, the distance-dependent interaction between tip and sample can be tuned via the electrolyte to be repulsive, repulsive and attractive, or attractive (Butt, 1991a,b, 1992a,b; Ducker et al., 1991). Once surfaces come into contact, their electron orbitals overlap, resulting in the strong Pauli repulsion.

The DLVO forces interacting between an AFM tip and purple membrane as a function of the vertical separation *z* and monovalent electrolyte concentration are shown in Fig. 3. We assumed two tip shapes. One tip was blunt, consisting of a global sphere (R_{glo} = 100 nm; Fig. 3 *a*) compatible with surface charge density measurements. The other tip, referred to here as the composite tip, consisted of a global sphere (R_{glo} = 100 nm) with a microscopic protrusion (R_{loc} = 2 nm) protruding 2 nm from the surface (Fig. 3, *b* and *c*) and was compatible with submolecular resolution achieved on biological samples (Engel et al., 1997). As the global sphere (Fig. 3 *a*) approaches the membrane surface, the electrostatic double-layer repulsion increases. At separations < 1 nm, the van der Waals attraction supersedes the double-layer repulsion. The degree of double-layer repulsion decreases with increasing electrolyte concentration. The calculations show that the van der Waals force dominates the electrostatic repulsion at separations < 1 nm. Thus, in a given separation range the global sphere (Fig. 3 *b*, solid lines) and the associated microscopic protrusion of the composite tip (Fig. 3 *b*, dotted lines) will interact differently with the sample (Eq. 4). The global sphere, separated by at least the height of the microscopic protrusion (2 nm), interacts predominantly with the purple membrane via long range electrostatic interactions (Fig. 3 *b*, solid lines). The microscopic protrusion, being closer to the membrane surface, interacts via short range forces such as van der Waals forces (Fig. 3 *b*, dotted line), Pauli repulsion, and, as recently calculated, hydration forces (Ho et al., 1998). The resultant force experienced by such a composite tip is displayed in Fig. 3 *c*. At identical electrolyte concentration, force plots of the high-resolution tip (Fig. 3 *c*) showed reduced maximum forces and a steeper peak shape in the electrostatic repulsion region compared to the blunt tip (Fig.

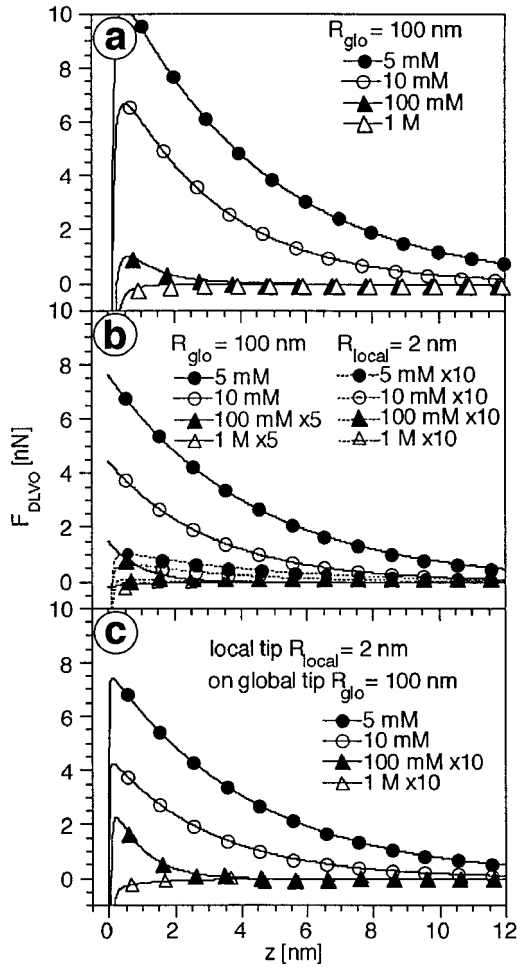

FIGURE 3 Electrostatic double-layer and van der Waals forces interacting between the AFM tip and the purple membrane surface as a function of the vertical separation z of the surfaces and the monovalent electrolyte concentration. (*a*) DLVO forces calculated for a macroscopic tip with 100-nm radius. (*b*) DLVO forces calculated for a microscopic tip with 2-nm radius (*dotted lines*) associated on the surface of a macroscopic sphere of 100 nm radius. The forces interacting on the microscopic half sphere (*dotted lines*) and forces interacting on the macroscopic sphere (*unbroken line*) are displayed separately. The surface of the microscopic tip was assumed to be 2 nm closer to the purple membrane surface than the surfaces of the macroscopic tip. Forces were calculated according to Eq. 4 (left side of the equation for macroscopic sphere, right side for microscopic half sphere). (*c*) Sum of the forces calculated in *b*. The surface charge densities taken for the calculations were -0.032 C/m^2 (Butt, 1991b) and -0.05 ± 0.025 C/m^2 (Butt, 1992b) for Si_3N_4 (tip) and purple membrane in water (around pH 7.0), respectively. The Hamaker constant for hydrocarbons in water was assumed to be 1×10^{-20} J (Butt et al., 1995). The notations "×5" and "×10" indicate that the curves were enhanced by a factor of 5 or 10, respectively.

3 *a*). At closer distances (< 0.3 nm) the microscopic protrusion jumps into attractive interaction with purple membrane. In the case of the blunt tip (Fig. 3 *a*) the vertical distance between maximum electrostatic repulsion and contact point ($z \rightarrow 0$ nm) lies between 0.51 nm and 0.61 nm for 5 mM and 100 mM monovalent electrolyte, respectively. In contrast, this vertical distance lies between 0.14 nm and 0.23 nm for 5 mM and 100 mM monovalent electrolyte, respectively, for the composite tip suitable for high-resolution imaging (Fig. 3 *c*).

Interpreting the calculations for high-resolution imaging

The calculated DLVO forces interacting between the AFM tip and the purple membrane provide new insight into the relationship between applied force and lateral resolution. When a force of 0.2 nN is applied in the presence of 10 mM monovalent salt (KCl), the protrusion of the composite AFM tip will be 9 nm away from the purple membrane surface (Fig. 3 *c*). Because the electrostatic repulsion is very smooth at this separation, relatively large changes in z cause small changes in force. Imaging under such conditions will not allow proteinous protrusions to be resolved with subnanometer resolution. To overcome this problem, one could apply a higher force during imaging. At an applied force of 0.6 nN the composite tip will be 6 nm away from the surface. Because of the shorter interaction lengths and the ascent of the interaction, it may then be possible to image the trigonal lattice of bacteriorhodopsin (a = 6.2 nm). To enhance the lateral resolution the force could be increased further. However, forces of more than 2 nN can disrupt the purple membrane during imaging (Müller et al., 1995a).

Alternatively, purple membrane can be imaged at a higher electrolyte concentration. According to our model, the protrusion of a composite tip is 1 nm away from the membrane surface at monovalent salt concentrations of 100 mM and an applied force of $\approx$ 0.1 nN, as required to prevent protein deformations (Müller et al., 1995b, 1997c) (Fig. 3 *c*). Hence, 100 mM and higher salt concentrations (calculated for neutral pH) will enable submolecular imaging of purple membrane at low applied force. However, if the salt concentration is sufficient, the electrostatic repulsion will be compensated by the van der Waals attraction (Fig. 3).

Stable imaging at constant forces requires the tip to be supported by electrostatic repulsion (Fig. 4). In its absence the tip will be pulled into the sample by van der Waals attraction and may deform the soft biomolecules even if the external force applied to the cantilever is 0.1 nN. Eq. 4 suggests that there is an optimum electrolyte concentration that provides sufficient repulsion of the cantilever to operate the microscope under stable conditions. At an applied force of 0.1 nN, a tip geometry as assumed in Fig. 3 *c*, and a surface charge density of -0.05 C/m^2, this concentration is between 100 and 200 mM monovalent counterions. Under these electrostatically balanced recording conditions, the microscopic protrusion of the composite tip is separated from the sample surface by about 1 nm (Fig. 3 *c*). In practice, the small repulsive interaction necessary for nondestructive imaging of the sample is detected by force curves and adjusted via the electrolyte.

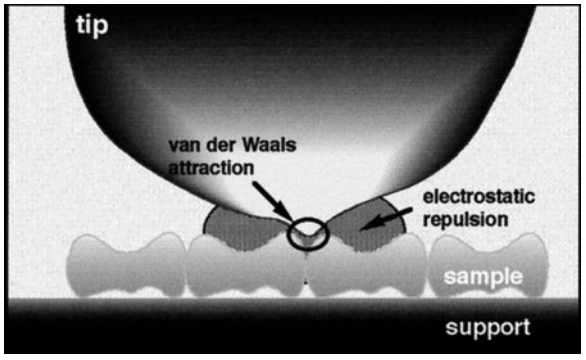

FIGURE 4 Forces interacting between AFM tip and sample in electrolyte solution. While the electrostatic double-layer force interacts via long-range forces with a larger area of the macromolecular assembly, the short-range van der Waals attraction and Pauli repulsion interacts with individual microscopic protrusions. The force effectively interacting at the tip apex is a composite of all interacting forces. If the electrostatic double-layer force is negligible ($F_{el} \approx 0$) or eliminated the effective force is equal to the sum of the applied force and the attractive van der Waals force $|F_{eff}| = |F_{appl} + F_{vdW}| > |F_{appl}|$. Being of opposite of sign, a sufficiently high electrostatic double-layer force will partially compensate for the applied force and the van der Waals attraction. Thus, under these conditions, the effective force is smaller than the applied force $|F_{eff}| = |F_{appl} + F_{el} + F_{vdW}| < |F_{appl}|$.

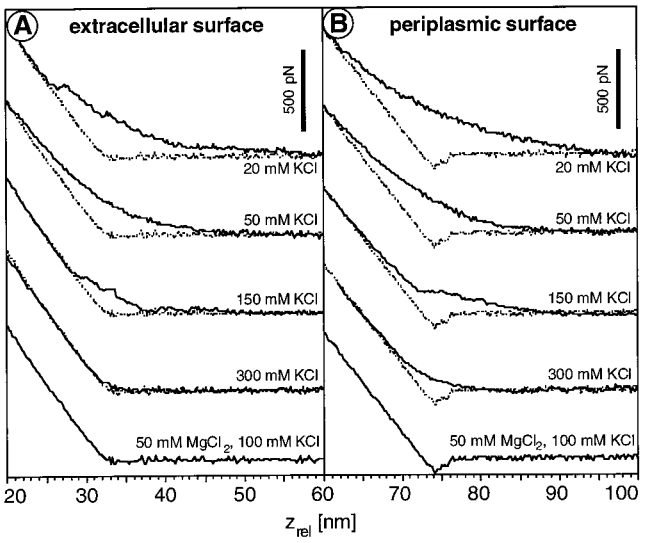

FIGURE 5 Force-distance-curves recorded on the extracellular (*a*) and periplasmic (*b*) surface of porin OmpF. The data were obtained for different electrolyte concentrations at constant pH (7.6). Force curves were recorded during the approach of sample and AFM tip. The dotted lines (. . . .) represent force-distance curves recorded on porin crystals without electrostatic repulsion (*bottom*). Conditions: scan frequency 1.97 Hz, scan range 50 nm (512 pixels).

High-resolution imaging

Porin OmpF from *E. coli* and HPI layer from *D. radiodurans* are the examples selected to substantiate the general validity of this straightforward approach. As a first step the electrolyte concentration must be adjusted to reduce, but not eliminate, the electrostatic double-layer repulsion between AFM tip and sample. To this end, force curves were recorded until electrolyte concentrations were found showing small repulsive forces of $\approx$ 0.1 nN. Under such conditions, high-resolution topographs were reproducibly acquired. To demonstrate the effect of insufficient electrostatic repulsion, topographs were recorded at electrolyte concentrations where no double-layer repulsion occurred.

Force curves taken on either the extracellular surface (Fig. 5 *a*) or the periplasmic surface (Fig. 5 *b*) of porin OmpF crystals showed the dependence of the electrostatic double-layer repulsion on the electrolyte concentration. At 20 mM KCl (5 mM Tris-HCl, pH 7.6) the force curves exhibited long-range repulsive forces similar to force curves recorded on purple membrane under the same conditions (compare Fig. 2). At an electrolyte concentration of 150 mM KCl (10 mM Tris-HCl, pH 7.6) force curves showed a repulsive force between 0.1 and 0.3 nN with an interaction length of about 5 nm. There were no significant differences between high-resolution topographs of the extracellular porin surface recorded in the trace and the retrace directions under this condition (Fig. 6 *a*). In both images trimeric domains of the relatively rough extracellular surface protruded 1.3 $\pm$ 0.2 nm (n = 78) from the lipid bilayer. Each domain exhibited two parallel subdomains that were separated by 1.3 $\pm$ 0.2 nm (n = 80). The width at half maximum height of the domains was 0.8 $\pm$ 0.1 nm (n = 92). Image averaging enhanced the structure of the porin trimer with its three domains surrounding a central vestibule (Fig. 6 *a*, insets). A lateral resolution of 0.8 nm was determined by the spectral signal-to-noise-ratio and the Fourier ring correlation function (Saxton and Baumeister, 1982; Schabert and Engel, 1994). However, on threefold symmetrization the substructure of the domains was lost, indicating both domain flexibility and various domain orientations relative to the scanning direction. This variability made the packing of two trimers per rectangular unit cell, dimensions a = 8.2 nm and b = 13.5 nm (Schabert and Engel, 1994), difficult to recognize in the unsymmetrized image.

Extracellular porin surfaces imaged at salt concentrations that allowed the double-layer repulsion to be eliminated (50 mM $MgCl_2$, 50 mM KCl, 10 mM Tris-HCl, pH 7.6), showed less pronounced structural details (Fig. 6 *b*). In addition, topographs obtained in the trace and retrace directions were different. The extracellular domains protruded 1.1 $\pm$ 0.3 nm (n = 93) above the lipid bilayer and appeared fuzzy. This pronounced flexibility caused the resolution of the substructures to be lost (Schabert et al., 1995), as can be seen clearly in correlation averages (Fig. 6 *b*, insets) of the porin trimers.

Because the periplasmic surface of porin OmpF has a higher surface charge density than the extracellular surface (Müller and Engel, 1997), 300 mM KCl (10 mM Tris-HCl, pH 7.6) was required to achieve an electrostatic double-layer repulsion of about 0.1 nN (Fig. 5 *b*). The high-resolution topographs obtained simultaneously in both scanning directions showed excellent agreement and revealed

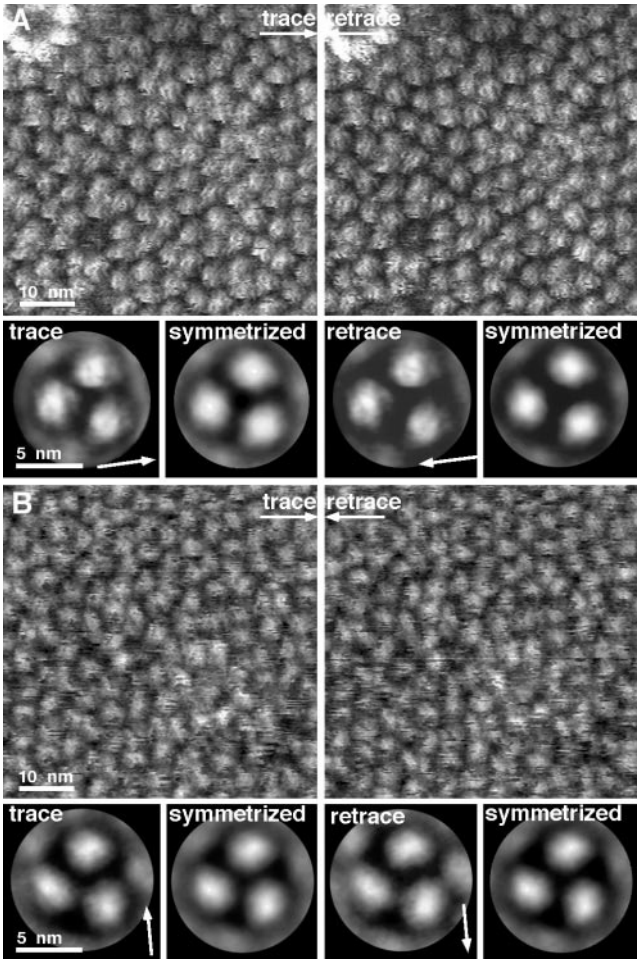

FIGURE 6 High-resolution topographs of the extracellular surface of native porin OmpF simultaneously recorded in trace and in retrace direction. (*a*) Extracellular surface imaged in 150 mM KCl (10 mM Tris-HCl, pH 7.6). Correlation averages ($n = 159$) are shown in the insets, with arrows indicating the scanning directions. The symmetrized averages (*insets*) showed RMS deviation from the threefold symmetry of 10.7%. (*b*) Extracellular surface imaged in 50 mM $MgCl_2$, 50 mM KCl (10 mM Tris-HCl, pH 7.6). Correlation averages ($n = 178$) are shown in the insets. The symmetrized averages (*insets*) showed RMS deviation from the threefold symmetry of 4.1%. Topographs were imaged at applied forces of 0.1 nN and at scan frequencies of 7.8 Hz. Full gray-level ranges: 2 nm (raw data) and 1.5 nm (*insets*).

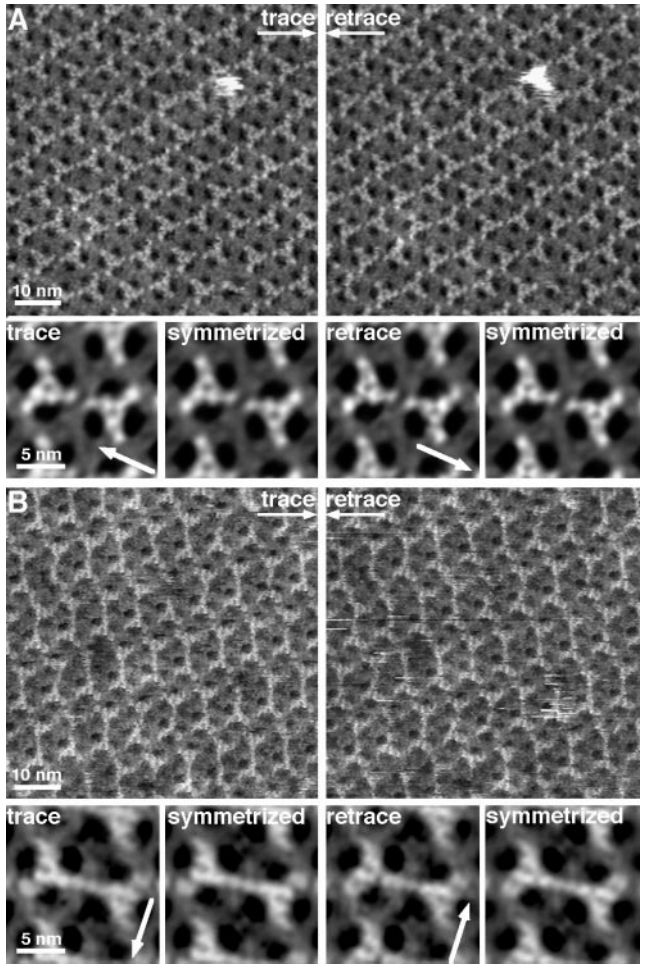

FIGURE 7 High-resolution topographs of the periplasmic surface of native porin OmpF simultaneously recorded in trace and in retrace direction. (*a*) Periplasmic surface imaged in 300 mM KCl (10 mM Tris-HCl, pH 7.6). Correlation averages ($n = 104$) are shown in the insets (arrows indicate the scanning direction). The symmetrized averages (*insets*) showed RMS deviation from the twofold symmetry of 2.6%. (*b*) Periplasmic surface imaged in 50 mM $MgCl_2$, 50 mM KCl (10 mM Tris-HCl, pH 7.6). Correlation averages ($n = 157$) are shown in the insets. The symmetrized averages (*insets*) showed RMS deviation from the twofold symmetry of 5.0%. Topographs were imaged at applied forces of 0.1 nN and at scan frequencies of 7.8 Hz. Full gray-level ranges: 1.2 nm (raw data) and 1 nm (*insets*).

the rectangular packing arrangement clearly (Fig. 7 *a*). The elliptical channels had a cross-section of a = 3.4 nm, b = 2.3 nm and a depth of 0.6 nm. These dimensions allowed the tip size to be estimated as 1.4 nm (Schabert and Engel, 1994), corroborating the tip model used in the theoretical analysis (Fig. 3). Subtle features such as the six protrusions arranged about the threefold symmetry axes were in excellent agreement with the atomic structure of OmpF porin (Cowan et al., 1992; Schabert et al., 1995). The protrusions exhibited a maximum height of 0.6 ± 0.1 nm ($n = 113$) above the lipid bilayer. Averaging of the unprocessed topographs enhanced the contrast of structural details, reduced the noise of the data (Fig. 7 *a*, insets), and allowed the lateral resolution to be determined as 0.6 nm by the Fourier ring correlation function (Saxton and Baumeister, 1982; Schabert and Engel, 1994). No significant morphological differences between averaged topographs recorded in the trace and the retrace directions could be detected. The maximum height differences between these averages were < 0.1 nm.

When the periplasmic porin surface was imaged at salt concentrations that fully compensated the double-layer repulsion (50 mM $MgCl_2$, 100 mM KCl, 10 mM Tris-HCl, pH 7.6), the topographs recorded in the trace and the retrace direction were different (Fig. 7). Structural details of the trimers were smeared out and showed less pronounced threefold symmetry (Fig. 7 *b*). The maximum height of structural details above the lipid layer was reduced to 0.4 ±

0.1 nm ($n = 124$). This effect is emphasized in the correlation averages of periplasmic porin trimers shown in Fig. 7 *b*. The domains were distorted along the fast scanning direction (arrows) and pushed onto the membrane by the AFM tip. Differences depended on the alignment of the trimers relative to the fast scan direction (Schabert and Engel, 1994; Schabert et al., 1995). Channel walls aligned parallel to the scanning direction were broadened, although perpendicularly aligned channel walls appeared thinner (compare to Fig. 7, *a* and *b*).

Force curves recorded on the outer surface of native HPI layer showed no electrostatic double-layer repulsion (Fig. 8), even at the low salt concentration of 20 mM KCl (5 mM Tris-HCl, pH 7.6). Nevertheless, topographs of the outer surface of the HPI layer imaged in 20 mM KCl (5 mM Tris-HCl, pH 7.6) were identical in the trace and the retrace directions (Fig. 9 *a*). The sixfold symmetry of the pore and of its connecting arms were clearly visible in the raw data. Submolecular structures such as the V-shaped protrusions (Baumeister et al., 1986) became pronounced in the averages (Fig. 9 *a*, insets). The height of the maximum protrusions over the connecting arms was 1.4 ± 0.2 nm ($n = 107$). Topographs of the outer surface acquired at high salt concentrations (50 mM $MgCl_2$, 300 mM KCl, 10 mM Tris-HCl, pH 7.6) exhibited a similar appearance (Fig. 9 *b*) to those recorded in 20 mM KCl (Fig. 9a), subtle features were enhanced by correlation averaging (Fig. 9, insets). The minor differences between these topographs (Fig. 9 *a* and *b*) resulted from differences in the tip shape.

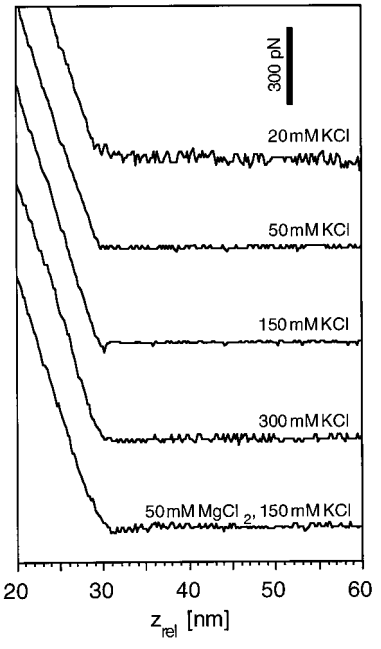

FIGURE 8 Force-distance curves recorded on the outer surface of the HPI layer. The data were obtained for different electrolyte concentrations at constant pH (7.6). Force curves were recorded during the approach of sample and tip. Conditions: scan frequency 1.97 Hz, scan range 50 nm (512 pixels).

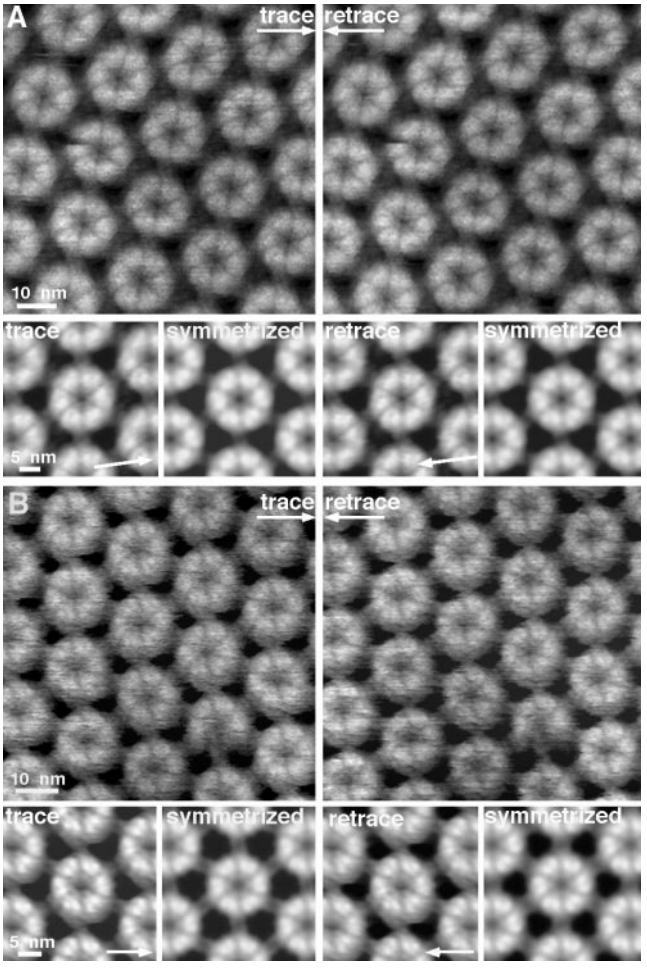

FIGURE 9 High-resolution topographs of the outer surface of the HPI layer simultaneously recorded in trace and retrace directions. (*a*) HPI layer imaged at 20 mM KCl (5 mM Tris-HCl, pH 7.6). Correlation averages ($n = 79$) are shown in the insets, with arrows indicating the scanning directions. The symmetrized averages (*insets*) showed RMS deviation from the sixfold symmetry of 2.8%. (*b*) HPI layer imaged at 50 mM $MgCl_2$, 300 mM KCl (10 mM Tris-HCl, pH 7.6). Correlation averages ($n = 87$) are shown in the insets. The symmetrized averages (*insets*) showed RMS deviation from the sixfold symmetry of 8.9%. Both topographs were imaged at applied forces of 0.1 nN and scan frequencies of 6.1 Hz. Full gray-level ranges: 4 nm (raw data) and 3 nm (*insets*).

DISCUSSION

In contrast to scanning in a humid environment or in vacuum, the interacting forces between the tip and the sample on scanning in buffer solution can be minimized to a few tens of picoNewtons. Although water has a dipole moment of 1.8 Debye and shields coulomb forces between two charged surfaces, electrolytes shield surface charges more effectively by building an electric double layer. When the AFM tip approaches the sample the respective double layers overlap to produce attractive (surfaces of opposite polarity) or repulsive (surfaces of equal polarity) interactions (Parsegian and Gingell, 1972). At closer distances (e.g., ≤ 1 nm) the attractive van der Waals force supersedes the electrostatic double-layer force, driving the tip into contact with

the sample. These forces are described by the DLVO theory, which has previously been used to estimate the force between the AFM tip and the sample (Butt, 1991a,b, 1992a,b; Ducker et al., 1991; Butt et al., 1995; Müller and Engel, 1997; Rotsch and Radmacher, 1997).

Here we use the DLVO theory to explain how high-resolution imaging of protein surfaces can routinely be achieved by adjusting the electrolyte concentration appropriately. The model is based on the experimentally determined global tip radius of 40–200 nm (Butt, 1992a,b) and local asperities whose radii have been estimated as about 2 nm (Schabert and Engel, 1994). As illuminated by Eqs. 3 and 4 and the corresponding graphs in Fig. 3, the electrostatic repulsion of the tip can be adjusted by the electrolytes to balance the force applied to the cantilever. During imaging in the contact mode the global AFM tip is then assumed to surf on a cushion of electrostatic repulsion (Fig. 4). However, force curves (Figs. 2, 5, and 8) together with the high-resolution topographs shown (Figs. 1, 6, 7, and 9) document the existence of sharp asperities (Müller and Engel, 1997). Such force curves are sensitive and simple experimental indicators which allow the electrolytes to be adjusted so that the sharp asperity at the end of the stylus is brought in close proximity of the sample when a preset force is applied to the tip. The force gradient in the repulsive regime determines the precision with which the tip-sample distance can be maintained by the servo. It is also an excellent indicator for the presence of organic contaminants, which in general give rise to long-range, weakly repulsive forces (Schabert and Engel, 1994).

The DLVO theory is based on the Poisson-Boltzmann equation describing the attraction of ions by homogeneously distributed surface charges and the tendency of ions to diffuse away. However, at separations $\leq$ 1 nm, which occur if the asperity of the AFM tip contours the sample surface, surface charges must be considered to interact as discrete charges. The finite ion size results in steric repulsions that may not be neglected. In the case of counterions the steric repulsion occurs between the surface-bound ions (i.e., the Stern layer). In addition, forces resulting from the bound water layers have been reported (Israelachvili, 1991). Such bound water layers can result in hydration forces between the AFM tip and the sample at separations $<$1 nm (Cleveland et al., 1995, see also Ho et al., 1998). However, such interactions have not yet been detected when examining biological samples. The comparison of AFM topographs of native proteins with their three-dimensional structures revealed by x-ray crystallography (Schabert et al., 1995; Fotiadis et al., 1998; Müller and Engel, 1998; Müller et al., 1998b) or electron microscopy (Karrasch et al., 1994; Walz et al., 1996; Fotiadis et al., 1998; Müller et al., 1999) showed only minimal differences.

High-resolution AFM imaging of a soft biological specimen requires small applied forces to minimize deformation artifacts (Müller et al., 1995b, 1997c; Engel et al., 1997). Provided that the AFM tip and sample have equal polarity, the effective force applied to proteinaceous substructures can be reduced below the applied force (Fig. 4). At applied forces slightly higher or equal to the electrostatic double-layer force, we can assume small protrusions of the composite tip to interact directly with the proteinous surface. The major part of the applied force will be distributed by longer range electrostatic forces over the macroscopic tip and an assembly of proteins (Fig. 4). In such cases one may describe the interaction between AFM tip and protein as electrostatically balanced.

Topographs recorded under electrostatically balanced conditions showed very good agreement between molecular details observed in the trace and retrace scanning direction suggesting negligible friction forces (Figs. 1 *a*, 6 *a*, and 7 *a*). The vertical resolution as estimated from standard deviation maps (Karrasch et al., 1994; Müller et al., 1998) was 0.1 nm, whereas the lateral resolution determined by the size of reproducibly imaged protrusions was 0.6 nm. It is interesting to relate this vertical resolution, which pertains to both variations in the protein and noise of the detector/servo system, to a vertical force. In general, cantilevers with a force constant of 0.1 nN were used, yielding a force of 10 pN at 0.1 nm deflection. In agreement with previous studies (Müller et al., 1995a,b, 1996a), molecular details of bacteriorhodopsin trimers were clearly visible, although the smallest details protruded only 0.1 nm above the lipid bilayer. On the periplasmic surface of porin OmpF, submolecular details of the trimer were reproducibly imaged. The fine structure of the flexible extracellular domains could also be imaged after adjustment of the electrolyte solution. These results underline the potential of the AFM to image native biological structures at subnanometer resolution in buffer solution. However, misadjustment of the electrolytes may lead to excessive van der Waals attraction. Depending on the effective force and the elasticity of the biological sample, friction and deformation effects may occur during imaging, as illustrated in Figs. 1 *b*, 5 *b*, 6 *b*, and 7 *b*. In these cases, topographs recorded in trace and retrace directions showed major differences, indicating considerable interaction between the AFM tip and soft biological sample, even at applied forces $\leq$ 0.1 nN. It should be noted that topographs recorded under these conditions resemble those recorded at applied forces $\geq$ 0.3–0.5 nN, but with correctly adjusted electrolytes (data not shown). Furthermore, such topographs are usually detoriated by tip artifacts. Most probably, the higher force applied locally to the biological sample not only broadens fragile structures, but also increases the contact area between the tip and the sample, which results in tip artifacts (Keller, 1991; Schwarz et al., 1994).

Electrostatic double-layer repulsion will also be absent if the sample surface is oppositely charged to the AFM tip. This effect was observed on the outer surface of the HPI layer (Fig. 8), and previously on DPPE double layers (Müller and Engel, 1997). Independent of the electrolyte concentration, the force curves showed an attractive interaction. Because the surface of the Si_3N_4 tip is negatively charged at pH $>$ 6 (Butt, 1992b) it may be concluded that the surface

charge of the outer surface of the HPI layer is either too small to be detected or positive (Müller and Engel, 1997). In the absence of repulsive electrostatic forces, the effective force during imaging the HPI layer is equal to the sum of the attractive force and the applied force (see Fig. 4). As a result, AFM topographs are barely influenced by the electrolyte (Fig. 9, *a* and *b*). Because the HPI layer is unusually stable (Baumeister et al., 1982, 1988), topographs recorded in different scanning directions do not show significant differences, and the submolecular V-shaped protrusions surrounding the pore are clearly visible after averaging (Fig. 9, insets).

As demonstrated here, the electrical double-layer interaction depends on surface charges of the AFM tip and the sample. Because of their individual properties biological samples exhibit individual surface charge densities. AFM tips, even from the same batch, can show different surface charge densities as well. Therefore, to achieve high-resolution images, it may be necessary to optimize the electrolyte conditions not only for the biological sample but also for each AFM tip used. Repulsive electrostatic double-layer forces are detected between charged surfaces showing the same polarity. In general, the salt concentration required to compensate for the electrical double-layer repulsion increases with the surface charge densities of tip and sample. It should be noted here that various other forces may interact between the AFM tip and the biological sample. The DLVO theory describes a simplified system, namely interactions via the electrostatic double-layer force and van der Waals attraction. It neglects other interactions such as those of chemical, hydration, hydrophobic, and steric origin. It will be highly interesting to extend the presented measurements to include the interplay of other interactions.

CONCLUSION

Topographs of native proteins with a lateral resolution of about 0.6 nm can reproducibly be acquired with the AFM. The AFM operator should control not only the applied force but also the electrostatic force interacting between tip and sample. This may be achieved by adjustment of the pH (polarity of charge) (Müller and Engel, 1997) and the ionic strength of the buffer solution. The effective force directly interacting between individual proteinous protrusions and the AFM tip can be reduced to fractions of the applied force. In this case, we describe the interaction between the AFM tip and protein as electrostatically balanced. In electrostatically balanced high-resolution topographs, lateral and vertical deformations are minimized.

We thank C. Möller for critical reading of the manuscript. We thank Dr. W. Baumeister for the HPI sample, Dr. G. Büldt for the purple membrane, and Dr. A. Hoenger for the OmpF porin crystals.

This work was supported by the Swiss National Research Foundation (Grant 4036–044062 to AE) and the Maurice E. Müller Foundation.

REFERENCES

Baumeister, W., M. Barth, R. Hegerl, R. Guckenberger, M. Hahn, and W. O. Saxton. 1986. Three-dimensional structure of the regular surface layer (HPI-layer) of *Deinococcus radiodurans*. *J. Mol. Biol.* 187: 241–253.

Baumeister, W., F. Karrenberg, R. Rachel, A. Engel, B. Ten Heggeler, and W. O. Saxton. 1982. The major cell envelope protein of *Micrococcus radiodurans* (R1). *Eur. J. Biochem.* 125:535–544.

Baumeister, W., I. Wildhaber, and H. Engelhardt. 1988. Bacterial surface proteins: some structural, functional and evolutionary aspects. *Biophys. Chem.* 29:39–49.

Binnig, G., C. F. Quate, and C. Gerber. 1986. Atomic force microscope. *Phys. Rev. Lett.* 56:930–933.

Bremer, A., C. Henn, A. Engel, W. Baumeister, and U. Aebi. 1992. Has negative stain still a place in biomacromolecular electron microscopy? *Ultramicroscopy* 46:85–111.

Butt, H.-J. 1991a. Electrostatic interaction in atomic force microscopy. *Biophys. J.* 60:777–785.

Butt, H.-J. 1991b. Measuring electrostatic, van der Waals, and hydration forces in electrolyte solutions with an atomic force microscope. *Biophys. J.* 60:1438–1444.

Butt, H.-J. 1992a. Electrostatic interaction in scanning probe microscopy when imaging in electrolyte solutions. *Nanotechnol.* 3:60–68.

Butt, H.-J. 1992b. Measuring local surface charge densities in electrolyte solutions with a scanning force microscope. *Biophys. J.* 63:578–582.

Butt, H.-J., M. Jaschke, and W. Ducker. 1995. Measuring surface forces in aqueous solution with the atomic force microscope. *Bioelect. Bioenerg.* 38:191–201.

Butt, H.-J., C. B. Prater, and P. K. Hansma. 1991. Imaging purple membranes dry and in water with the atomic force microscope. *J. Vac. Sci. Technol.* B 9:1193–1197.

Cleveland, J. P., T. E. Schäffer, and P. K. Hansma. 1995. Probing oscillatory hydration potentials using thermal-mechanical noise in an atomic force microscope. *Phys. Rev. B* 52: R8692–R8695.

Cowan, S. W., T. Schirmer, G. Rummel, M. Steiert, R. Ghosh, R. A. Pauptit, J. N. Jansonius, and J. P. Rosenbusch. 1992. Crystal structures explain functional properties of two *E. coli* porins. *Nature.* 358:727–733.

Czajkowsky, D. M., M. J. Allen, V. Elings, and Z. Shao. 1998b. Direct visualization of surface charge in aqueous solution. *Ultramicroscopy.* 74:1–5.

Czajkowsky, D. M., S. Sheng, and Z. Shao. 1998a. Staphylococcal α-hemolysin can form hexamers in phospholipid bilayers. *J. Mol. Biol.* 276:325–330.

Dammer, U., M. Hegner, D. Anselmetti, P. Wagner, M. Dreier, W. Huber, and H. J. Güntherodt. 1996. Specific antigen/antibody interactions measured by force microscopy. *Biophys. J.* 70:2437–2441.

Dammer, U., O. Popescu, P. Wagner, D. Anselmetti, H. J. Güntherodt, and G. N. Misevic. 1995. Binding strength between cell adhesion proteoglycans measured by atomic force microscopy. *Science.* 267:1173–1175.

Drake, B., C. B. Prater, A. L. Weisenhorn, S. A. C. Gould, T. R. Albrecht, C. F. Quate, D. S. Cannell, H. G. Hansma, and P. K. Hansma. 1989. Imaging crystals, polymers, and processes in water with the atomic force microscope. *Science.* 243:1586–1588.

Ducker, W. A., T. J. Senden, and R. M. Pashley. 1991. Direct measurements of colloidal forces using an atomic force microscope. *Nature.* 353:239–241.

Engel, A. 1991. Biological applications of scanning probe microscopy. *Annu. Rev. Biophys. Chem.* 20:79–108.

Engel, A., C.-A. Schoenenberger, and D. J. Müller. 1997. High-resolution imaging of native biological sample surfaces using scanning probe microscopy. *Curr. Opin. Struct. Biol.* 7:279–284.

Florin, E.-L., V. T. Moy, and H. E. Gaub. 1994. Adhesion forces between individual ligand-receptor pairs. *Science.* 264:415–417.

Fotiadis, D., D. J. Müller, G. Tsiotis, L. Hasler, P. Tittmann, T. Mini, P. Jenö, H. Gross, and A. Engel. 1998. Surface analysis of the photosystem I complex by electron and atomic force microscopy. *J. Mol. Biol.* 283:83–94.

Ho, R., J. Y. Yuan, and Z. Shao. 1998. Hydration force in the atomic force microscope: a computational study. *Biophys. J.* 75:1076–1083.

Hoenger, A., R. Ghosh, C.-A. Schoenenberger, U. Aebi, and A. Engel. 1993. Direct in situ structural analysis of recombinant outer membrane proteins expressed in an OmpA-deficient mutant *Escherichia coli* strain. *J. Struct. Biol.* 111:212–221.

Hoh, J. H., G. E. Sosinsky, J.-P. Revel, and P. K. Hansma. 1993. Structure of the extracellular surface of the gap junction by atomic force microscopy. *Biophys. J.* 65:149–163.

Israelachvili, J. 1991. Intermolecular and Surface Forces. Second Edition. Academic Press Limited, London.

Jap, B. K., M. Zulauf, T. Scheybani, A. Hefti, W. Baumeister, U. Aebi, and A. Engel. 1992. 2D crystallization: from art to science. *Ultramicroscopy.* 46:45–84.

Karrasch, S., R. Hegerl, J. Hoh, W. Baumeister, and A. Engel. 1994. Atomic force microscopy produces faithful high-resolution images of protein surfaces in an aqueous environment. *Proc. Natl. Acad. Sci. USA.* 91:836–838.

Keller, D. 1991. Reconstruction of STM and AFM images distorted by finite-size tips. *Surf. Sci.* 253:353–364.

Lee, G. U., L. A. Chrisey, and R. J. Colton. 1994a. Direct measurements of the forces between complementary strands of DNA. *Science.* 266: 771–773.

Lee, G. U., D. A. Kidwell, and R. J. Colton. 1994b. Sensing discrete streptavidin-biotin interactions with atomic force microscopy. *Langmuir.* 10:354–357.

Mou, J., D. M. Czajkowsky, S. Sheng, R. Ho, and Z. Shao. 1996. High resolution surface structure of *E. coli* GroES oligomer by atomic force microscopy. *FEBS Lett.* 381:161–164.

Mou, J. X., J. Yang, and Z. F. Shao. 1995. Atomic force microscopy of cholera toxin B-oligomers bound to bilayers of biologically relevant lipids. *J. Mol. Biol.* 248:507–512.

Moy, V. T., E.-L. Florin, and H. E. Gaub. 1994. Adhesive forces between ligand and receptor measured by AFM. *Coll. Surf.* A93:343–348.

Müller, D. J., and A. Engel. 1998. pH and voltage induced structural changes of porin OmpF explain channel closure. *J. Mol. Biol*. (in press)

Müller, D. J., D. Fotiadis, and A. Engel. 1998. Mapping flexible protein domains at subnanometer resolution with the AFM. *FEBS Lett.* 430: 105–111.

Müller, D. J., H.-J. Sass, S. Müller, G. Büldt, and A. Engel. 1999. Surface structures of native bacteriorhodopsin depend on the molecular packing arrangement in the membrane. *J. Mol. Biol.* In press.

Müller, D. J., and A. Engel. 1997. The height of biomolecules measured with the atomic force microscope depends on electrostatic interactions. *Biophys. J.* 73:1633–1644.

Müller, D. J., M. Amrein, and A. Engel. 1997a. Adsorption of biological molecules to a solid support for scanning probe microscopy. *J. Struct. Biol.* 119:172–188.

Müller, D. J., A. Engel, and M. Amrein. 1997b. Preparation techniques for the observation of native biological systems with the atomic force microscope. *Biosens. Bioelect.* 12:867–877.

Müller, D. J., A. Engel, J. Carrascosa, and M. Veléz. 1997c. The bacteriophage ø29 head-tail connector imaged at high resolution with atomic force microscopy in buffer solution. *EMBO J.* 16:101–107.

Müller, D. J., C.-A. Schoenenberger, F. Schabert, and A. Engel. 1997d. Structural changes of native membrane proteins monitored at subnanometer resolution with the atomic force microscope. *J. Struct. Biol.* 119: 149–157.

Müller, D. J., C. A. Schoenenberger, G. Büldt, and A. Engel. 1996a. Immuno-atomic force microscopy of purple membrane. *Biophys. J.* 70:1796–1802.

Müller, D. J., W. Baumeister, and A. Engel. 1996b. Conformational change of the hexagonally packed intermediate layer of *Deinococcus radiodurans* imaged by atomic force microscopy. *J. Bacteriol.* 178: 3025–3030.

Müller, D. J., G. Büldt, and A. Engel. 1995a. Force-induced conformational change of bacteriorhodopsin. *J. Mol. Biol.* 249:239–243.

Müller, D. J., F. A. Schabert, G. Büldt, and A. Engel. 1995b. Imaging purple membranes in aqueous solutions at subnanometer resolution by atomic force microscopy. *Biophys. J.* 68:1681–1686.

Oberhauser, A. F., P. E. Marszalek, H. P. Erickson, and J. M. Fernandez. 1998. The molecular elasticity of the extracellular matrix protein tenascin. *Nature.* 393:181–185.

Oesterhelt, D., and W. Stoeckenius. 1974. Isolation of the cell membrane of *Halobacterium halobium* and its fraction into red and purple membrane. *Methods Enzymol.* 31:667–678.

Parsegian, V. A., and D. Gingell. 1972. On the electrostatic interaction across a salt solution between two bodies bearing unequal charges. *Biophys. J.* 12:1192–1204.

Putman, C. A. J., K. van der Werft, B. G. de Grooth, N. F. van Hulst, J. Greve, and P. K. Hansma. 1992. A new imaging mode in the atomic force microscopy based on the error signal. *SPIE.* 1639:198–204.

Rief, M., M. Gautel, F. Oesterhelt, J. M. Fernandez, and H. E. Gaub. 1997. Reversible unfolding of individual titin immunoglobulin domains by AFM. *Science.* 276:1109–1112.

Rotsch, C., and M. Radmacher. 1997. Mapping local electrostatic forces with the atomic force microscope. *Langmuir.* 13:2825–2832.

Saxton, W. O., and W. Baumeister. 1982. The correlation averaging of a regularly arranged bacterial cell envelope protein. *J. Microsc.* 127: 127–138.

Saxton, W. O., T. J. Pitt, and M. Horner. 1979. Digital image processing: the semper system. *Ultramicroscopy.* 4:343–354.

Schabert, F. A., C. Henn, and A. Engel. 1995. Native *Escherichia coli* OmpF porin surfaces probed by atomic force microscopy. *Science.* 268:92–94.

Schabert, F. A., and A. Engel. 1994. Reproducible acquisition of *Escherichia coli* porin surface topographs by atomic force microscopy. *Biophys. J.* 67:2394–2403.

Schwarz, U. D., H. Haefke, P. Reimann, and H. J. Güntherodt. 1994. Tip artifacts in scanning force microscopy. *J. Microsc.* 173:183–197.

Shao, Z., J. Mou, D. M. Czajkowsky, J. Yang, and J.-Y. Yuan. 1996. Biological atomic force microscopy: what is achieved and what is needed. *Adv. Phys.* 45:1–86.

Walz, T., P. Tittmann, K. H. Fuchs, D. J. Müller, B. L. Smith, P. Agre, H. Gross, and A. Engel. 1996. Surface topographies at subnanometer-resolution reveal asymmetry and sidedness of aquaporin-1. *J. Mol. Biol.* 264:907–918.

Wilson, J. A., and A. D. Yoffe. 1969. The transition metal dichalcogenides: discussion and interpretation of the observed optical, electrical and structural properties. *Advanc. Phys.* 18:193–335.